Heterogeneity in VEGF Receptor-2 Mobility and Organization on the Endothelial Cell Surface Leads to Diverse Models of Activation by VEGF

Bruno da Rocha-Azevedo[1], **Sungsoo Lee**[1,3], **Aparajita Dasgupta**[1], **Anthony R. Vega**[1,2], **Luciana R. de Oliveira**[1], **Tae Kim**[1], **Mark Kittisopikul**[1,4], **Zachariah A. Malik**[1], **Khuloud Jaqaman**[1,2,5,*]

[1]Department of Biophysics, UT Southwestern Medical Center, Dallas, TX 75390, USA

[2]Lyda Hill Department of Bioinformatics, UT Southwestern Medical Center, Dallas, TX 75390, USA

[3]Present address: Tunneling Nanotube Research Center and Division of Life Sciences, Korea University, Seoul 02841, South Korea

[4]Present address: Scientific Computing, Janelia Research Campus, Howard Hughes Medical Institute, Ashburn, VA 20147, USA

[5]Lead Contact

SUMMARY

The dynamic nanoscale organization of cell surface receptors plays an important role in signaling. We determine this organization and its relation to activation of VEGF receptor-2 (VEGFR-2), a critical receptor tyrosine kinase in endothelial cells (ECs), by combining single-molecule imaging of endogenous VEGFR-2 in live ECs with multiscale computational analysis. We find that surface VEGFR-2 can be mobile or exhibit restricted mobility and be monomeric or non-monomeric, with a complex interplay between the two. This basal heterogeneity results in heterogeneity in the sequence of steps leading to VEGFR-2 activation by VEGF. Specifically, we find that VEGF can bind to monomeric and non-monomeric VEGFR-2 and that, when binding to monomeric VEGFR-2, its effect on dimerization depends on the mobility of VEGFR-2. Our study highlights the dynamic and heterogeneous nature of cell surface receptor organization and the need for multiscale, single-molecule-based analysis to determine its relationship to receptor activation and signaling.

Graphical Abstract

In Brief

da Rocha-Azevedo et al. show that VEGFR-2 exhibits mobility and interaction heterogeneity on the endothelial cell surface. The sequence of steps leading to VEGFR-2 activation by VEGF depends on the basal state of VEGFR-2. Thus, there is not one model but multiple co-existing models of VEGFR-2 activation by VEGF.

INTRODUCTION

The dynamic nanoscale organization of cell surface receptors plays an important role in their interactions with ligands and downstream effectors and, consequently, cell signaling (Casaletto and McClatchey, 2012; Garcia-Parajo et al., 2014; Githaka et al., 2016; Jaqaman et al., 2011; Sungkaworn et al., 2017; Treanor et al., 2010; Zhou et al., 2017). This organization emerges from the complex regulation of receptor mobility, localization, and interactions by many factors. It is thus imperative to study this organization and its relation to signaling in a receptor's native cellular environment with minimal system perturbation. Compared with studies in reconstituted systems or model cell systems, studies in the native cellular environment reveal which behaviors indeed occur and how they relate to each other and to receptor function.

Live-cell single-molecule imaging (SMI) is a powerful approach to observe molecules in their native environment with high resolution in space and time (Liu et al., 2015; Xia et al., 2013). However, individual receptor behavior, be it localization, mobility, or interactions, is generally heterogeneous and stochastic, especially under unperturbed conditions (Freeman et al., 2018; Jaqaman et al., 2011). Receptor behavior and its related cellular-level processes also span a wide range of spatial and temporal scales (Jaqaman et al., 2016). Computational and statistical analysis approaches are critical to tackle these challenges and attain a full understanding of the dynamic organization of receptors and its relation to signaling.

We employed SMI with a pipeline of automated image analysis and quantitative, multiscale data analysis to determine the dynamic organization of vascular endothelial growth factor receptor-2 (VEGFR-2) in its native plasma membrane of endothelial cells (ECs) and to link this organization to ligand binding and receptor activation. VEGFR-2, a receptor tyrosine kinase, is the main receptor in ECs for VEGF-A (VEGF in brief). VEGF is the major promoter of angiogenesis in health and disease (Ferrara et al., 2003; Karaman et al., 2018; Olsson et al., 2006; Simons et al., 2016; Terman et al., 1992). For our studies, we employed primary human microvascular ECs (pHMVECs), which play a central role in angiogenesis.

The mechanism of VEGFR-2 activation by VEGF is currently under debate. The canonical model, derived primarily from cell-free systems, is that VEGF binds to VEGFR-2 monomers, leading to their dimerization, activation by *trans*-autophosphorylation, and signaling (Ruch et al., 2007; Simons et al., 2016). However, recent work in plasma membrane-derived vesicles from Chinese hamster ovary (CHO) cells expressing exogenous VEGFR-2 provides evidence that VEGFR-2 can dimerize in the absence of ligand and that VEGF binding to pre-existing dimers leads to dimer conformational changes that enable receptor activation (Sarabipour et al., 2016). Our study allowed us to determine the interplay between these two models as part of providing a comprehensive, quantitative characterization of the so far unknown dynamic nanoscale organization of VEGFR-2 on the EC surface.

RESULTS

VEGFR-2 Exhibits Mobility and Interaction Heterogeneity on the Surface of Unstimulated pHMVECs

To image individual VEGFR-2 molecules in their native plasma membrane environment, we labeled early-passage, unstimulated pHMVECs with a low concentration of primary Fab fragments that bound to the extracellular domain of VEGFR-2 (without altering activation; Figures S1A and S1B), followed by secondary Fab fragments conjugated to Rhodamine Red-X (RRX). We used total internal reflection fluorescence microscopy (TIRFM) to acquire 10-Hz/20-s SMI streams at 37°C focused on the bottom cell surface (Figure 1A; Video S1), followed by multiple-particle detection and tracking (Jaqaman et al., 2008) to obtain the labeled receptor tracks (Video S2). The number of detected particles per frame was ~200 in an area that is about half the bottom cell surface, suggesting that ~10% of surface VEGFR-2 molecules were labeled (the total number of surface VEGFR-2 molecules in pHMVECs has been measured to be ~7,700; Imoukhuede and Popel, 2011).

Approximately 75% of the labeled molecules were still visible at the end of each stream (Figures S1C–S1F).

Through diffusion analysis based on frame-to-frame displacements (Jaqaman et al., 2016), we characterized each VEGFR-2 track with an effective diffusion coefficient D. D is "effective" because it describes the movement of VEGFR-2 molecules at the 100-ms timescale of SMI streams, implicitly reflecting the effects of confinement or other restrictions on VEGFR-2 diffusion. D followed a bimodal distribution, allowing us to set a data-driven threshold (0.032 μm^2/s) for VEGFR-2 surface mobility classification (Figure 1B). Using this threshold, ~35% of the tracks were classified as mobile, with mean D_{mobile} = 0.185 μm^2/s, and ~65% were classified as restricted, with mean $D_{restricted}$ = 0.008 μm^2/s (Figure 1C; Video S3). Less than 3% of VEGFR-2 tracks exhibited directed movement (Figure S1G; classification obtained by moment scaling spectrum analysis; Jaqaman et al., 2011; Vega et al., 2018). Thus, the imaged receptors were over-whelmingly on the cell surface; internalized receptors in early endosomes would exhibit directed movement (Granger et al., 2014).

We also noticed heterogeneity in detected particle intensities (Figure 1A) and merging and splitting events between detected particle tracks (Figure 1D; Video S4; Jaqaman et al., 2008). The apparent dissociation rate constant calculated from merging and splitting events (de Oliveira and Jaqaman, 2019) was in the range of 0.19–0.26/s. This was about one order of magnitude lower than that expected from coincidental overlap because of molecules diffusing and passing by each other (Figure 1E). It was also an order of magnitude higher than the photobleaching rate (~0.02/s; Figures S1C–S1F); thus, its estimation was mini-mally affected by photobleaching. Therefore, the captured merging and splitting events largely reflected transient interactions of the imaged VEGFR-2 molecules. Given the resolution limit of the light microscope, these transient interactions could reflect unligated dimerization or oligomerization (Bogdanovic et al., 2009; Chung et al., 2010; Hern et al., 2010; Hiroshima et al., 2012, 2018; Kasai et al., 2018; Lin et al., 2012; Low-Nam et al., 2011; Mischel et al., 2002; Sarabipour et al., 2016), indirect interactions through other receptors (Simons et al., 2016), or clustering within nanodomains such as clathrin-coated pits or caveolae (Labrecque et al., 2003; Lampugnani et al., 2006). To describe the non-monomeric state of VEGFR-2 in a neutral manner, we will use the term "assembly state."

Estimation of the apparent assembly state n of the tracked VEGFR-2 particles from their intensities and sequence of merging and splitting events (de Oliveira and Jaqaman, 2019) revealed a distribution of states, with more restricted particles than mobile particles in non-monomeric states (Figure 1F). A large fraction of the tracked particles had $n = 1$, confirming that VEGFR-2 labeling and imaging were at the single-molecule level. Yet a substantial fraction had $n > 1$. Because ~20% of the secondary Fab fragments had more than one fluorophore (Figure 1F, "labeling with highly diluted Fab concentration"), this analysis could not reveal the absolute assembly state of a detected particle. However, the fraction of VEGFR-2 with $n > 1$ was 41% for mobile particles and 48% for restricted particles, both significantly greater than 20% ($p < 10^{-15}$; Figure 1F).

To further investigate the relationship between VEGFR-2 mobility and interactions, next we focused on the dynamic particle merging and splitting events (Figure 1D; Video S4). We found that mobile particles had a higher probability of merging, especially with other mobile particles (Figure 1G). At the same time, although particles could exhibit either mobility mode after merging, merging events enriched the restricted mode (Figure 1H). This was consistent with the observation that restricted particles had an overall higher assembly state than mobile particles (Figure 1F). For particles that stayed mobile after merging, there was some reduction in D (Figure 1I). Splitting exhibited the converse relationships (Figures 1J and 1K). In contrast to the merging probability, the apparent dissociation rate constant was the same for both mobility modes (Figure 1E).

These analyses indicate that VEGFR-2 molecules in the plasma membrane of live, unstimulated pHMVECs exhibit heterogeneity in mobility and assembly state. On average, the mobile mode of VEGFR-2 promotes interactions, and interactions enrich the restricted subpopulation. However, the relationships between mobility, interactions, and assembly state are not one-to-one at the single-molecule level.

VEGF Reduces VEGFR-2 Mobility on the pHMVEC Surface over Multiple Timescales

To determine how VEGF affects the dynamic nanoscale organization of VEGFR-2, shedding light on the role of this organization in VEGFR-2 signaling, we performed SMI of VEGFR-2 after stimulating pHMVECs with 2 nM VEGF (VEGF-A$_{165}$). Because the effect of VEGF is time dependent and unfolds over minutes (Figures S2A and S2B; Ferrara et al., 2003; Hamdollah Zadeh et al., 2008; Lampugnani et al., 2006; Simons et al., 2016), which is an order of magnitude slower than the timescale of our SMI streams (10-Hz/20-s), we devised a "time course" imaging and analysis strategy that allowed us to study single-molecule properties on timescales relevant to cellular processes. We imaged multiple cells within the course of an experiment (1 cell every ~3 min for ~25 min total time), keeping track of their acquisition time relative to addition of VEGF (if added; usually just before imaging the second cell in a time course; Figure 2A). For data analysis (time course analysis [TCA]), multiple time courses were aligned by the time point of VEGF addition or time 0 (i.e., first cell) in the case of no stimulation. This allowed us to group cells based on time (~15 cells per 5-min time interval, with 1,000–1,500 VEGFR-2 tracks each) to investigate their single-molecule properties over longer timescales than captured by any individual SMI stream. There was no systematic variation in single-molecule properties between individual time courses representing any particular condition (Figures S2C–S2E). Also, addition of liquid at the microscope did not significantly alter single-molecule behavior in unstimulated cells (Figures S2F–S2H).

Focusing first on VEGFR-2 mobility, our analysis revealed that VEGF led to a gradual decrease in the probability of the mobile mode, starting 5–10 min after VEGF addition (Figures 2B and 2C). In contrast, D_{mobile} exhibited an almost immediate drop upon VEGF addition, down to a mean of ~0.135 μm^2/s (Figure 2D). $D_{restricted}$ did not change (Figure 2E). These results indicate that VEGF has a fast and slow effect on VEGFR-2 mobility. The slow effect occurs on the timescale of the cellular signaling response (Figures S2A and S2B), whereas the fast effect is almost immediate.

VEGF Enhances the Probability of Interactions between Restricted VEGFR-2 Molecules

Next we investigated the effect of VEGF stimulation on VEGFR-2 merging events to determine whether VEGF promotes VEGFR-2 interactions on the pHMVEC surface, as described by the canonical model of VEGFR-2 activation (Ruch et al., 2007; Simons et al., 2016). Interestingly, we found that VEGF stimulation increased the probability of merging for restricted-restricted particle pairs but not for events involving mobile particles (Figure 2F). In fact, the overall rate of merging between VEGFR-2 particles decreased over time in the presence of VEGF (Figure 2G). This rate was for all particles, akin to an overall association rate (but only for the labeled subset of VEGFR-2 molecules). This reduction in merging rate reflected the fact that most merging events involved mobile particles (as reflected by their much higher merging probability; Figure 2F), whose fraction and effective diffusion coefficient decreased in the presence of VEGF (Figures 2C and 2D).

These results suggest that the canonical model applies to interactions between restricted VEGFR-2 molecules, most likely because restricted receptors are limited to sampling a small area and, thus, have a low chance of encountering other restricted receptors on their own. In this case, VEGF, which is a constitutive dimer (Ferrara et al., 2003), can act as an attractor that brings receptors together. In contrast, mobile receptors have a much higher chance of encountering other receptors on their own, and VEGF does not seem to increase their interaction probability.

VEGF Binds to VEGFR-2 of All Assembly States on the pHMVEC Surface

The above analysis provides evidence that the canonical model applies to a subset of VEGF-VEGFR-2 binding events on the surface of pHMVECs. To investigate the extent to which the alternative model (i.e., VEGF binding to pre-existing VEGFR-2 dimers; Sarabipour et al., 2016) applies in the native context, we performed simultaneous 2-color TIRFM of VEGFR-2 (labeled as above) and VEGF (conjugated to Atto488) (Figures S3A and S3B; Video S5). We labeled VEGF at a relatively high density (40% of the 2 nM dose was labeled) to increase the chance of observing colocalization between a labeled VEGFR-2 molecule and a labeled VEGF molecule. We detected single particles of VEGF using Gaussian mixture model fitting (Jaqaman et al., 2008; Video S6). Then, after tracking VEGFR-2 particles, we associated VEGFR-2 tracks in each frame with co-localized VEGF particles (primary-secondary channel analysis) (Figure 3A). There was minimal bleedthrough between the two channels (Figures S3C and S3D), lending confidence to the captured VEGFR-2-VEGF associations. With this, we analyzed the interactions, assembly state, and mobility of VEGFR-2 in the context of its association with VEGF at the single-molecule level.

The single-molecule mobility trends upon VEGF association were consistent with the ensemble mobility trends (see Figures 3B and 3C versus Figures 2C and 2D). Interestingly, a larger fraction of restricted VEGFR-2 particles was associated with VEGF than mobile VEGFR-2 particles, implying that VEGF had a higher probability to bind to VEGFR-2 already in the restricted mode (Figure 3D). We reasoned that this could be because of the overall higher assembly state of restricted particles (Figure 1F), which could increase the avidity of VEGF-VEGFR-2 binding (the dissociation constant for VEGF binding to

monomeric and dimeric VEGFR-2 has been estimated to be 5–10 nM and 0.05–0.2 nM, respectively; Fuh et al., 1998; King and Hristova, 2019; for comparison, we stimulated the cells with a 2 nM dose of VEGF).

The apparent assembly state of VEGFR-2 particles positive for labeled VEGF was indeed higher than that of VEGFR-2 particles negative for labeled VEGF, and it increased over time (Figure 3E). However, this analysis did not inform us whether VEGF bound to monomers that then associated with each other or whether it bound to pre-existing non-monomers. To distinguish between these two scenarios, we measured the waiting time from the start of each VEGFR-2 track to its moment of labeled VEGF association. We found a wide range of wait times for tracks of any assembly state (Figure 3F), indicating that many association events occurred with pre-existing VEGFR-2 non-monomers. Focusing on the dynamic VEGFR-2 merging events, we also found that, among the merging events that were positive for labeled VEGF, in half of them, VEGF association occurred only after the merge of the two VEGFR-2 particles (Figure 3G).

These analyses provide evidence that a fraction of VEGF associates with pre-existing VEGFR-2 non-monomers on the pHMVEC surface, consistent with the alternative model of VEGF-VEGFR-2 binding and activation (Sarabipour et al., 2016). This indicates that the canonical and alternative models of VEGF-VEGFR-2 binding and activation co-exist in the native context. Our data also provide evidence that these two models co-exist with yet a third, "in between" model, where VEGF binds to a VEGFR-2 monomer that then dimerizes with another VEGFR-2 monomer but without any ligand-induced enhancement (Figure 2F).

VEGF Stabilizes VEGFR-2 Interactions

The simultaneous 2-color imaging experiments of VEGFR-2 and VEGF also allowed us to assess the effect of VEGF association on the stability of VEGFR-2 interactions, by comparing the apparent dissociation rate constant of interaction events positive for VEGF with that of events negative for VEGF. We found that the apparent dissociation rate constant of interaction events positive for labeled VEGF was about half that of interaction events negative for labeled VEGF (Figure 3H), indicating that association with VEGF stabilizes VEGFR-2 interactions. This stabilization most likely underlies the overall increase in VEGFR-2 assembly state upon VEGF addition (Figure 3E) in spite of the decrease in the overall merging rate (Figure 2G).

The Drop in D_{mobile} upon VEGF Stimulation Is Upstream of Phosphorylation, and the Shift toward the Restricted Mode Is Downstream

VEGF-VEGFR-2 binding leads to tyrosine phosphorylation of the intracellular domain of VEGFR-2. Thus, the observed effects of VEGF on VEGFR-2 behavior could be from VEGF binding itself or from VEGFR-2 phosphorylation and activation. To distinguish between these two scenarios, we performed SMI followed by TCA for pHMVECs in the presence of the VEGFR phosphorylation inhibitor AAL-993 (Manley et al., 2002), using a 30-nM dose for 1 h (Figures S2A and S2B). These experiments also allowed us to investigate the role of VEGFR-2 phosphorylation in unstimulated cells because previous studies have provided evidence of VEGFR-2 phosphorylation resulting from unligated dimerization (Sarabipour et

al., 2016). Although weak, we did observe a slight reduction in VEGFR-2 phosphorylation in the presence of AAL-993 in unstimulated pHMVECs (Figures S2A and S2B).

Diffusion analysis and TCA revealed that the two mobility modes of VEGFR-2 were conserved in the presence of AAL-993, but now with a shift toward the mobile mode, in unstimulated and VEGF-stimulated cells (Figures 4A–4C). Parallel to the increase in mobile VEGFR-2 particles, there was a mild increase in the merging rate of VEGFR-2 in the absence and presence of VEGF (Figures S3E and S3F). However, the almost immediate drop in D_{mobile} upon VEGF stimulation was insensitive to the presence of AAL-993 (Figure 4D).

These observations indicate that VEGFR-2 phosphorylation upon VEGF binding plays a role in the shift in mobility mode from mobile to restricted, which, in fact, occurs on the timescale of the cellular signaling response (see Figure 2C versus Figures S2A and S2B). The almost immediate drop in D_{mobile} upon VEGF binding is, however, upstream of VEGFR-2 phosphorylation.

DISCUSSION

Through live-cell SMI and a pipeline of automated image and data analysis, we exposed the dynamic nanoscale organization of VEGFR-2 in its native plasma membrane and shed light on the interplay between this organization, ligand binding, and receptor activation at the single-molecule level. We found that VEGFR-2 molecules on the surface of pHMVECs exhibit heterogeneity in mobility and assembly state, where they can be mobile or restricted, both of which can be monomeric or non-monomeric, even in unstimulated cells. On average, the mobile mode promotes VEGFR-2 encounters and interactions, which, in turn, enrich the restricted mode. The relationship, however, is not one-to-one; many molecules remain mobile after interacting with each other, and, conversely, some restricted molecules appear to be monomeric. Although the propensity for interactions depends on the mobility mode, the apparent dissociation rate constant of non-monomeric states does not.

Our work provides evidence that unligated VEGFR-2 molecules, expressed endogenously on the EC surface and with the full slew of native regulatory factors, exist in non-monomeric states, consistent with previous work with CHO cell membranes (Sarabipour et al., 2016). Because of sub-stoichiometric labeling, what we observe is most likely only the lower bound of the fraction of VEGFR-2 in non-monomeric states. Our single-molecule analyses indicate that VEGF binds to monomeric and non-monomeric VEGFR-2, providing evidence of the coexistence of the canonical model of VEGFR-2 activation by VEGF (VEGF-induced dimerization; Ruch et al., 2007; Simons et al., 2016), the alternative model (VEGF binding to VEGFR-2 pre-dimers; Sarabipour et al., 2016)), and an "in between" model. In the "in between" model, VEGF binds to a VEGFR-2 monomer (contrary to the alternative model), which then dimerizes with another VEGFR-2 monomer but without any ligand-induced enhancement (contrary to the canonical model), eventually leading to activation.

The specific model followed by any particular VEGFR-2 molecule depends on its mobility mode and assembly state prior to VEGF binding. For molecules in a monomeric state, restricted molecules would follow the canonical model of VEGF-enhanced dimerization

when interacting with other restricted molecules, whereas mobile molecules and restricted molecules interacting with mobile molecules would follow the "in between" model. The balance between the different coexisting models most likely depends on the dose of VEGF to which the cells are exposed, because the avidity of VEGF binding to dimeric VEGFR-2 is ~2 orders of magnitude higher than that of binding to monomeric VEGFR-2 (Fuh et al., 1998; King and Hristova, 2019). It is also conceivable that factors (internal or external to the cell) that alter the dynamic nanoscale organization of VEGFR-2 can modulate the responsiveness of ECs to VEGF.

The partitioning of VEGFR-2 into two mobility modes is most likely due to many factors. We found that VEGFR-2 phosphorylation promotes the restricted mode, even in unstimulated cells. Phosphorylation in the absence of stimulation could be due to unligated dimerization (Sarabipour et al., 2016) or association with Src family kinases (Chen et al., 1999; Jin et al., 2003; Tzima et al., 2005). Thus, the restricted mode is at least partially due to interactions with downstream effectors and scaffolds (Labrecque et al., 2003; Lampugnani et al., 2006; Olsson et al., 2006), even when transient in the absence of ligand. Interestingly, the timescale of the VEGF-induced shift from mobile to restricted mode parallels the timescale of VEGFR-2 activation by VEGF. In contrast, D_{mobile} is independent of VEGFR-2 phosphorylation and exhibits a fast (almost immediate) drop upon VEGF addition. This change is most likely due to conformational changes in VEGFR-2 upon VEGF binding (Sarabipour et al., 2016) and/or association of VEGFR-2 with co-receptors through VEGF (Gelfand et al., 2014; Somanath et al., 2009).

Our experiments and analyses demonstrate a complex relationship between receptor mobility and interactions, leading to distinct ligand effects and receptor activation steps based on the mobility of individual receptors. This highlights the need to study receptors at the single-molecule level in their native cellular environment. It also highlights the need for developing analytical approaches that not only characterize individual receptor properties but also derive relationships between them at the single-molecule level (Hiroshima et al., 2018; Low-Nam et al., 2011) (versus at an ensemble level). The explicit characterization of each receptor's mobility, assembly, and ligation state separately from each other and then using transients in these properties to derive relationships between them at the single-molecule level was instrumental in our ability to identify the multiple co-existing models of VEGFR-2 activation. Furthermore, multiscale imaging and analysis approaches that bridge the gap between the molecular and cellular scales are critical for linking receptor behaviors to their emergent cellular outcomes.

STAR★METHODS

RESOURCE AVAILABILITY

Lead Contact—Further information and requests for resources should be directed to and will be fulfilled by the Lead Contact, Khuloud Jaqaman (khuloud.jaqaman@utsouthwestern.edu).

Materials Availability—This study did not generate new unique reagents.

Data and Code Availability—The data generated during this study are available upon request. All custom code written for the purposes of this study is available on GitHub (under https://github.com/kjaqaman), as listed in the Key Resources Table.

EXPERIMENTAL MODEL AND SUBJECT DETAILS

This study employed early passage (P4-P7) primary cultures of human dermal microvascular endothelial cells isolated from neonatal foreskin (HD-MVECn from LifeLine Cell Technology, Frederick, MD; referred to as pHMVECs throughout our study). Cell type was authenticated by the supplier by ensuring that cells tested positive for Van Willebrand Factor (a marker for endothelial cells) and negative for smooth muscle α-actin. Cells were grown in VascuLife VEGF-Mv culture medium at 37°C + 5% CO2, and passaged every 48 hours upon reaching 70%–90% confluency, following the supplier's instructions.

METHOD DETAILS

Cell culture and plating—Early passage (P4-P7) HD-MVECn cells (LifeLine Cell Technology, Frederick, MD) were grown in VascuLife VEGF-Mv culture medium for 48 h at 37°C + 5% CO2 until reaching 70%–90% confluency. For stimulation, cells were treated with 2 nM VEGF-A$_{165}$ (Genscript, Piscataway, NJ) at time points indicated in time course analysis or western blots. To inhibit VEGFR-2 phosphorylation, cells were incubated with 30 nM of AAL-993 (MilliporeSigma, Burlington, MA), starting 1 h before the experiments and continuing for the duration of the experiments. For SMI experiments, 5.4×10^4 cells were plated 18 h prior to imaging on base/acid cleaned glass bottom dishes (14 mm glass diameter with glass thickness of 0.17 mm (#1.5), MatTek, Ashland, MA) pre-coated for 45 minutes with 10 μg/ml fibronectin (MilliporeSigma).

Preparation of anti-VEGFR-2 Fab fragments and fluorescence labeling of VEGF—The Pierce Mouse IgG1 Fab and F(ab')2 Preparation Kit (Thermo Scientific, Waltham, MA) was used to generate Fab fragments from the anti-human VEGFR-2 mouse monoclonal antibody EIC (Abcam, Cambridge, MA). To reach optimal generation of Fab fragments, 500 μg of antibody were digested with immobilized ficin for 3h at 37°C, and, after the purification steps, the product was concentrated in a 10 kDa cut-off column. VEGF was conjugated with Atto488 through the succinimidyl ester group of the dye, using the Atto protein labeling kit following the manufacturer's directions (MilliporeSigma). The dye-to-protein ratio obtained from the labeled VEGF was 0.4, as determined by spectrophotometry.

VEGFR-2 single molecule labeling—Plated cells were washed once with wash buffer (HBSS + 1 mM HEPES and 0.1% NGS), blocked for 15 min at 37°C in blocking buffer (1% BSA, 5% NGS in wash buffer) and then incubated for 15 min with 0.2 μg/ml of primary anti-VEGFR-2 Fab fragments at 15°C. After 3 washes (1 min, RT), dishes were incubated for 15 min at RT in the dark with 2 μg/ml of a Rhodamine-Red-X (RRX)-conjugated goat anti-mouse secondary Fab fragment (Jackson ImmunoResearch, West Grove, PA). After 3 washes (1 min, RT), dishes were incubated with imaging buffer at 37°C (containing Oxyfluor 1%, Glucose 0.45%, Trolox 2 nM) in order to reduce photobleaching. The purpose of the initial incubation with primary Fab fragments at 15°C, then incubation with secondary Fab fragments at RT, and then finally incubation with imaging buffer at 37°C was to

minimize receptor and Fab fragment internalization during the labeling period while gently bringing the cells back to 37°C for imaging.

To determine the number of fluorophores per secondary Fab fragment, the labeling procedure described above was followed, but with a much lower concentration of primary Fab fragments (0.1 μg/ml) and secondary Fab fragments (0.045 μg/ml). These experiments and subsequent analyses (as described in the main text) indicated that 80% of the secondary Fab fragments binding to primary Fab fragments were conjugated to one fluorophore, 17% were conjugated to two fluorophores, and the remaining 3% were conjugated to ≥ 3 fluorophores (Figure 1F). This distribution of fluorophores yielded an average of ~1.23 fluorophores per Fab fragment (0.8*1+0.17*2+0.03*3), which was close to the company's estimate of 1.3 fluorophores per Fab fragment for the lot of Fab fragments employed in our study.

Live-cell single-molecule imaging (SMI)—Cells were imaged at 37°C using an S-TIRF system (Spectral Applied Research, via BioVision Technologies, Exton, PA) mounted on a Nikon Ti-E inverted microscope with Perfect Focus and a 60x/1.49 NA oil TIRF objective (Nikon Instruments, Melville, NY). The system was equipped with two Evolve EMCCD cameras (Photometrics, Tucson, AZ) for one-color or simultaneous two-color imaging, registered to within 1–3 pixels of each other. A custom 3x tube lens was employed to achieve an 89 nm pixel size in the recorded image. Illumination by a 561 nm diode pumped solid state laser (Cobolt) and/or a 488 nm diode laser (Coherent) was achieved through an ILE laser merge module (Spectral Applied Research), with 561 nm and 488 nm laser power of 13.2 mW and 3.65 mW, respectively, at the coverslip. The penetration depth was set to 80 nm via the Diskovery platform control (Spectral Applied Research). Videos were acquired with MetaMorph (Molecular Devices, San Jose, CA) in stream mode at 100 ms per frame (i.e., 10 Hz sampling) for 200 frames, using an EM gain of 100. Temperature and humidity were maintained using an environment chamber (Okolab, Otaviano, Italy), maintaining cell viability for the duration of the experiments (Trypan Blue staining indicated 75% viability of cells plated on dishes whether exposed or not to imaging buffer for 30 min). For time courses stimulated with VEGF or Atto488-VEGF, 1 mL imaging buffer containing VEGF or Atto488-VEGF was added at the microscope just before imaging the second cell in a time course (final concentration of VEGF or Atto488-VEGF was 2 nM). Every SMI stream was preceded by a brightfield snapshot of the imaged cell region in order to visually check cell viability and to delineate the cell mask (manually) for any ensuing analysis.

Western blotting—After cell treatment (or not) with VEGF, Atto488-VEGF, and/or AAL-993 for the indicated times, cells were treated with lysis buffer (Mammalian-PE LB Buffer, GoldBio, St. Louis, MO) and a protease/phosphatase inhibitor cocktail (Thermo Scientific) for 10 min on ice under agitation. Lysates were collected after centrifugation, re-suspended in Laemmli sample buffer, and heated (90°C for 10 min). Samples were loaded in 4%–15% gradient SDS-PAGE Mini-PROTEAN TGX gels (Bio-Rad, Hercules, CA). Proteins were transferred to PVDF membranes (100 V / 1 h / 4°C) and blocked using 5% BSA in TBST. Rabbit anti-human antibodies against VEGFR-2 (55B11, 1/2000 dilution, Cell Signaling, Danvers, MA), Y1175 phospho-VEGFR-2 (19A10, 1/1000 dilution, Cell

Signaling), actin (1/1000 dilution, MilliporeSigma) and/or GAPDH (1/2500 dilution, Abcam) were incubated with membranes for 18h at 4°C. Goat anti-Rabbit secondary antibody conjugated with HRP (1/5000 dilution, Thermo Scientific) was incubated for 1 h at RT in the dark. Protein bands were detected by chemiluminescence using Clarity Western ECL Substrate (BioRad), and densitometric analyses were made using Image Lab (BioRad).

Computing environment—All image and data analysis tasks were performed in MATLAB 2018b and more recent versions (The MathWorks, Natick, MA). All employed code and software packages are compatible with MATLAB 2018b on a Linux 64-bit operating system. Imaging streams were loaded into MATLAB using Bio-Formats (Linkert et al., 2010).

Particle detection and tracking—Particle detection and tracking were performed using u-track (Jaqaman et al., 2008; https://github.com/DanuserLab/u-track). The detection and tracking parameters, listed in the tables below, were optimized based on the performance diagnostics included in u-track and visual inspection of the resulting detection and tracking. The mean particle localization precision, as estimated during the Gaussian mixture-model fitting step (Jaqaman et al., 2008), was 20 nm for VEGFR-2 in one-channel streams, and 26 nm and 33 nm for VEGFR-2 and VEGF, respectively, in two-channel streams. The median track duration for tracks lasting at least 5 frames (as needed for mobility analysis as described next) was 19 frames (i.e., 1.9 s). In all the following analyses, only detections and tracks inside the cell mask (determined from the brightfield image as described above) were employed.

U-track detection parameters (Gaussian Mixture-Model Fitting). Shown are the parameters with non-default values for any of the three conditions, based on u-track Version 2.2.1.

	1-channel imaging: VEGFR-2	2-channel imaging: VEGFR-2	2-channel imaging: VEGF
Gaussian standard deviation	1.33 pixels	1.33 pixels	1.33 pixels
Local maxima detection: Use rolling window time-averaging	No	Yes (windows 1 and 3 frames) [*]	Yes (windows 1 and 3 frames) [*]
Local maxima detection: α-value for comparison with local background	0.05	0.05 (window 1), 0.1 (window 3)	0.1 (both windows)
Gaussian mixture-model fitting at local maxima: Do iterative Gaussian mixture-model fitting	Yes	Yes	Yes
Gaussian mixture-model fitting at local maxima: α-value for residuals test	0.01	0.01	0.05
Gaussian mixture-model fitting at local maxima: α-value for amplitude test	0.05	0.05	0.1
Gaussian mixture-model fitting at local maxima: α-value for distance test	0.01	0.05	0.1

[*] A rolling window of 1 frame implies no time-averaging. A rolling window of 3 frames means averaging over the current frame, the frame before, and the frame after.

U-track tracking parameters. Shown are the parameters with non-default values, based on u-track Version 2.2.1.

	VEGFR-2 from 1- or 2-channel imaging
Overall: Do segment merging	Yes
Overall: Do segment splitting	Yes
Frame-to-frame linking: Brownian search radius upper bound	10 pixels
Frame-to-frame linking: Multiplication factor for Brownian search radius calculation	4
Gap closing, merging and splitting - general: Brownian search radius upper bound	10 pixels
Gap closing, merging and splitting - general: Multiplication factor for Brownian search radius calculation	4
Gap closing, merging and splitting - general: Scaling power to expand Brownian search radius	0.25
Gap closing, merging and splitting - general: Use nearest neighbor distance to expand Brownian search radius	No
Gap closing, merging and splitting - merging & splitting: Search radius lower bound	3 pixels
Gap closing, merging and splitting - merging & splitting: For an end/start, the possibility of merging/splitting is allowed only if there is no possibility of gap closing	Yes [*]
Gap closing, merging and splitting - birth & death: Birth and death cost	Derived from gap closing and merging/splitting cost formulae

[*] Limiting merging and splitting events to segment ends and starts that do not have the possibility of gap closing helps with distinguishing between molecular interactions and particles passing by each other.

Mobility analysis—The effective diffusion coefficient D of each VEGFR-2 particle was calculated from its mean square frame-to-frame displacement r^2 (mean obtained by averaging over all consecutive frames of its track, i.e., assuming ergodicity) and localization precision σ (also averaged over all frames of its track), as previously described (Jaqaman et al., 2016; https://github.com/kjaqaman/diffModesF2F):

$$D = \frac{r^2}{4} - \sigma^2 \tag{1}$$

Only tracks with duration 5 frames were included in the mobility analysis, through which each track was described with its own D (Jaqaman et al., 2016). As described in the main text, the D values of all individual particles followed a bimodal distribution under all conditions (Figure 4A). Thus, each VEGFR-2 track was classified as either mobile or restricted, based on whether its D value was greater than or less than the classification threshold, respectively. The classification threshold was taken as 0.032 μm^2/s for all conditions in one-channel streams (at the trough between the two modes). In the case of two-channel data, the distribution of VEGFR-2 effective diffusion coefficients was shifted slightly toward higher values, most likely because of the reduced localization precision in these data due to lower signal-to-noise ratio. Thus the classification threshold was shifted to 0.046 μm^2/s in two-channel data, to coincide with the trough between the two modes in this condition.

Estimation of apparent assembly state and apparent dissociation rate constant—The apparent assembly state for the labeled subset of VEGFR-2 molecules was calculated from the particle intensities and their sequence of merging and splitting events as described in Equation 2 and Equation 3 in de Oliveira and Jaqaman (2019) (https://github.com/kjaqaman/FISIK). The assembly state is "apparent" because by definition only labeled molecules are visualized and counted. This analysis required the mean intensity of an individual fluorophore, which was estimated per SMI stream by decomposing the distribution of detected particle intensities in the first 5 frames of the stream into a superposition of multiple modes corresponding to 1, 2, 3, etc. fluorophores (Jaqaman et al., 2011). Each mode was taken as a log-normal distribution, where the mean and standard deviation of mode n were (approximately) n times those of mode 1 (Mutch et al., 2007). The fit was achieved using least-squares, and the number of modes was determined using the Bayesian Information Criterion for model selection (Jaqaman and Danuser, 2006). With this, the mean individual fluorophore intensity was obtained per SMI stream, and then used to estimate the apparent assembly state of each particle as described in de Oliveira and Jaqaman (2019). The apparent dissociation rate constant per apparent assembly state was then calculated from the transitions between apparent assembly states as described in Equation 4 in de Oliveira and Jaqaman (2019). For clarity, it is important to point out here that these analyses were limited to the labeled subset of receptors, and did not use the full analytical framework developed in de Oliveira and Jaqaman (2019).

Calculation of merging probability and merging rate—These calculations were analogous to the stochastic treatment of chemical reactions. Specifically, in stochastic chemical kinetics (Gillespie, 1977; Lecca, 2013), a reaction

$$A + B \rightarrow C$$
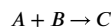
is characterized by a constant c_1 such that $c_1 \Delta t$ = probability of any individual pair of A and B molecules to react in a time interval Δt. Then, if there are N_A and N_B molecules of type A and B, respectively, the combined probability of the reaction occurring in Δt, P_{comb}, is defined as:

$$P_{comb} = c_1 \Delta t N_A N_B. \tag{2}$$

In the special case of two identical molecules reacting, say molecules of type A, the combined probability of the reaction occurring in Δt, P_{comb}^*, is defined as:

$$P_{comb}^* = c_1 \Delta t \frac{N_A(N_A - 1)}{2}. \tag{3}$$

In both cases, the combined probability to react is defined as the probability for an individual pair to react ($c_1 \Delta t$) multiplied by the number of possible pairs. The constant c_1 is equivalent to the association rate constant in deterministic chemical kinetics (Gillespie, 1977; Lecca, 2013).

In a manner analogous to Equation 3, the merging rate r_{merge}, equivalent to c_1, was defined as:

$$r_{merge} = \frac{2N_{merge}}{N_{part}(N_{part} - 1)\Delta t}, \tag{4}$$

where N_{merge} = average number of merges per frame, N_{part} = average number of detected particles per frame, and Δt = time interval between consecutive frames. N_{merge} is a generalization of P^*_{comb} in Equation 3, as N_{merge} could be > 1 (whereas a probability cannot be).

The merging probabilities per motion mode pair, equivalent to $c_1 \Delta t$ in Equation 2 and Equation 3, were calculated in a similar manner. The merging probabilities between two mobile particles ($p_{merge,mob-mob}$) and between two restricted particles ($p_{merge,mob-mob}$) were based on Equation 3. Using x to represent *mob* or *res*, they were defined as:

$$p_{merge,x-x} = \frac{2N_{merge,x-x}}{N_{part,x}(N_{part,x} - 1)}, \tag{5}$$

where $N_{merge,x-x}$ = average number of merges per frame involving two particles with motion mode x, and $N_{part,x}$ = average number of detected particles per frame with motion mode x. The merging probability between one mobile particle and one restricted particle ($p_{merge,mob-mob}$) was based on Equation 2, and was defined as:

$$p_{merge,mob-res} = \frac{N_{merge,mob-res}}{N_{part,mob}N_{part,res}}, \tag{6}$$

where $N_{merge,mob-res}$ = average number of merges per frame involving one mobile and one restricted particle, and $N_{part,mob}$ and $N_{part,res}$ = average number of mobile and restricted particles per frame, respectively.

Primary-secondary channel analysis of VEGFR-2-VEGF association in two-channel imaging streams—For this analysis, the VEGFR-2 channel was considered the primary channel, in which VEGFR-2 particles were both detected and tracked, and the VEGF channel was considered the secondary channel, in which VEGF particles were only detected. Then, VEGFR-2-VEGF association was determined in two steps:

First, in each frame, the colocalization between VEGFR-2 and VEGF particles was determined by solving a linear assignment problem (Jonker and Volgenant, 1987) based on their relative positions, with a maximum allowed distance of 4 pixels (~350 nm). This maximum distance accounted for both the particles' localization precision (0.3–0.4 pixels on average) and the 1–3 pixel registration shift between the two cameras acquiring the two-channel images. After this first step, each VEGFR-2 track had a 1/0 association flag with VEGF in each frame.

Second, the association history per track was used to distinguish spurious associations from reliable ones. Specifically, a VEGFR-2 track was considered to reliably associate with

VEGF if the association history satisfied the following two conditions: (i) its association flag = 1 in at least three frames; and (ii) its association flag = 1 for at least 10% of the frames between its first frame of VEGF association and last frame of VEGF association (e.g., if the first frame of VEGF association is frame 11, and the last frame of VEGF association is frame 50, then the association flag should be 1 for at least $0.1 \times 40 = 4$ frames). For tracks considered to reliably associate with VEGF, the average fraction of time associated with VEGF was 57% of their duration (34% of the tracks were associated with VEGF for 90% of their duration).

With this, each VEGFR-2 track reliably associated with VEGF was divided into the interval before VEGF association and the interval during VEGF association for further analysis as needed (e.g., VEGFR-2 mobility). Note that if the VEGFR-2-VEGF association was lost in some later frame, a VEGFR-2 track would then also have an interval after VEGF association, but this was not used for any analysis in our study.

Time course analysis (TCA): data aggregation strategies—For time course analysis, two data aggregation strategies were taken, based on the amount of data available per individual cell to calculate the single-molecule property of interest.

Strategy 1.: For single-molecule properties with sufficient data points per cell, primarily properties related to receptor mobility, single-molecule properties were calculated per cell (e.g., mean D_{mobile} per cell), and then individual cell measurements were grouped by time interval for time course analysis. A time interval of 5 minutes was used, as it provided enough individual cell measurements per time interval (10–20) to minimize measurement noise, while allowing for sufficient temporal sampling to capture temporal trends. In this case, the figures display the individual cell measurements, and the mean value and standard error of the mean for the grouped cells per time interval (e.g., Figure 2C).

Strategy 2.: For single-molecule properties with insufficient data points per cell, particularly properties related to receptor interactions (as seen in Figure 1G, the merging probability on the order of 10^{-5}/particle), the individual cell measurements could exhibit relatively large fluctuations from cell to cell. In this case, the grouping was done at the level of the tracks within the cells of interest. Specifically, the single-molecule property (e.g., apparent dissociation rate constant) was calculated from all the tracks combined, and the standard deviation of that property was calculated via bootstrapping (using 100 bootstrap samples). This standard deviation was equivalent to the standard error of the mean of individual cell measurements. In this case, the figures display the property as calculated from the combined tracks and the standard deviation from bootstrapping (e.g., Figures 3E and 3G).

When such analysis was performed on unstimulated cells, all cells were grouped together, as VEGFR-2 properties did not vary over time in unstimulated cells (Figures 2C–2E and 2G). On the other hand, when such analysis was performed on stimulated cells, a time interval of 10 minutes was used, thus separating the early and late trends in VEGFR-2 behavior upon VEGF addition (0–10 min and 10–20 min after VEGF addition, respectively). A 10-minute time interval was used instead of a 5-minute time interval (as done in Strategy 1 above) in order to further reduce measurement noise.

QUANTIFICATION AND STATISTICAL ANALYSIS

Dataset information—The statistical details of all experiments (number of independent repeats, number of cells imaged per repeat, and number of tracks used for analysis) are reported in the figure legends. Statistical tests are described in the figure legends, and in more detail below.

Statistical tests—Below is a description of the various statistical tests used for comparing single-molecule properties:

For properties where individual cell measurements were available in the time course analysis (data aggregation strategy 1, described in the previous section), the properties were compared between conditions for each time interval using a one-sided t test (based on the individual cell measurements within the time interval). In this case, significant differences are indicated by asterisks above each time interval (e.g., Figure 2C).

In cases where all per-interval comparisons were not significant (p value > 0.05), the full time course was compared between conditions using a paired, one-sided t test. Specifically, each time course was represented by its series of mean values per time interval, and the series of two conditions were compared using a paired t test. In other words, time courses without VEGF stimulation had 5 data points (e.g., Figure 4B), while time courses with VEGF stimulation had 4 data points (corresponding to the time intervals after VEGF addition; e.g., Figure 4C). In this case, significant differences are indicated by a square bracket and an asterisk at the end of the time course plot (e.g., Figures 4B and 4C). The reasoning behind this test was that temporal persistence in a trend (e.g., one condition being always higher than the other) might indicate a significant difference, even if the difference is not strong enough to detect for each time interval separately.

For properties calculated by first combining all tracks for a group of cells (data aggregation strategy 2, described in the previous section), the property standard deviation was obtained via bootstrapping, and was equivalent to the standard error of the mean of individual cell measurements. In this case, to compare conditions (or time intervals) 1 and 2, with property values μ_1 and μ_2, and variances v_1 and v_2, the difference between them, $\mu_1 - \mu_2$, was taken to follow $N(0, v_1+v_2)$. This distribution was then used to calculate the p value to assess the difference between the two conditions (or time intervals). In this case, significant differences are indicated by asterisks above each time interval in the time course, or otherwise as described in the figure legends.

Supplementary Material

Refer to Web version on PubMed Central for supplementary material.

ACKNOWLEDGMENTS

REFERENCES

Bogdanovic E, Coombs N, and Dumont DJ (2009). Oligomerized Tie2 localizes to clathrin-coated pits in response to angiopoietin-1. Histochem. Cell Biol 132, 225–237. [PubMed: 19424712]

Casaletto JB, and McClatchey AI (2012). Spatial regulation of receptor tyrosine kinases in development and cancer. Nat. Rev. Cancer 12, 387–400. [PubMed: 22622641]

Chen KD, Li YS, Kim M, Li S, Yuan S, Chien S, and Shyy JYJ (1999). Mechanotransduction in response to shear stress. Roles of receptor tyrosine kinases, integrins, and Shc. J. Biol. Chem 274, 18393–18400. [PubMed: 10373445]

Chung I, Akita R, Vandlen R, Toomre D, Schlessinger J, and Mellman I (2010). Spatial control of EGF receptor activation by reversible dimerization on living cells. Nature 464, 783–787. [PubMed: 20208517]

de Oliveira LR, and Jaqaman K (2019). FISIK: Framework for the Inference of In Situ Interaction Kinetics from Single-Molecule Imaging Data. Biophys. J 117, 1012–1028. [PubMed: 31443908]

Ferrara N, Gerber HP, and LeCouter J (2003). The biology of VEGF and its receptors. Nat. Med 9, 669–676. [PubMed: 12778165]

Freeman SA, Vega A, Riedl M, Collins RF, Ostrowski PP, Woods EC, Bertozzi CR, Tammi MI, Lidke DS, Johnson P, et al. (2018). Transmembrane Pickets Connect Cyto- and Pericellular Skeletons Forming Barriers to Receptor Engagement. Cell 172, 305–317.e10. [PubMed: 29328918]

Fuh G, Li B, Crowley C, Cunningham B, and Wells JA (1998). Requirements for binding and signaling of the kinase domain receptor for vascular endothelial growth factor. J. Biol. Chem 273, 11197–11204. [PubMed: 9556609]

Garcia-Parajo MF, Cambi A, Torreno-Pina JA, Thompson N, and Jacobson K (2014). Nanoclustering as a dominant feature of plasma membrane organization. J. Cell Sci 127, 4995–5005. [PubMed: 25453114]

Gelfand MV, Hagan N, Tata A, Oh WJ, Lacoste B, Kang KT, Kopycinska J, Bischoff J, Wang JH, and Gu C (2014). Neuropilin-1 functions as a VEGFR2 co-receptor to guide developmental angiogenesis independent of ligand binding. eLife 3, e03720. [PubMed: 25244320]

Gillespie DT (1977). Exact stochastic simulation of coupled chemical reactions. J. Phys. Chem 81, 2340–2361.

Githaka JM, Vega AR, Baird MA, Davidson MW, Jaqaman K, and Touret N (2016). Ligand-induced growth and compaction of CD36 nanoclusters enriched in Fyn induces Fyn signaling. J. Cell Sci 129, 4175–4189. [PubMed: 27694211]

Granger E, McNee G, Allan V, and Woodman P (2014). The role of the cytoskeleton and molecular motors in endosomal dynamics. Semin. Cell Dev. Biol 31, 20–29. [PubMed: 24727350]

Hamdollah Zadeh MA, Glass CA, Magnussen A, Hancox JC, and Bates DO (2008). VEGF-mediated elevated intracellular calcium and angiogenesis in human microvascular endothelial cells in vitro are inhibited by dominant negative TRPC6. Microcirculation 15, 605–614. [PubMed: 18800249]

Hern JA, Baig AH, Mashanov GI, Birdsall B, Corrie JE, Lazareno S, Molloy JE, and Birdsall NJ (2010). Formation and dissociation of M1 muscarinic receptor dimers seen by total internal reflection fluorescence imaging of single molecules. Proc. Natl. Acad. Sci. USA 107, 2693–2698. [PubMed: 20133736]

Hiroshima M, Saeki Y, Okada-Hatakeyama M, and Sako Y (2012). Dynamically varying interactions between heregulin and ErbB proteins detected by single-molecule analysis in living cells. Proc. Natl. Acad. Sci. USA 109, 13984–13989. [PubMed: 22891299]

Hiroshima M, Pack CG, Kaizu K, Takahashi K, Ueda M, and Sako Y (2018). Transient Acceleration of Epidermal Growth Factor Receptor Dynamics Produces Higher-Order Signaling Clusters. J. Mol. Biol 430, 1386–1401. [PubMed: 29505756]

Imoukhuede PI, and Popel AS (2011). Quantification and cell-to-cell variation of vascular endothelial growth factor receptors. Exp. Cell Res 317, 955–965. [PubMed: 21185287]

Jaqaman K, and Danuser G (2006). Linking data to models: data regression. Nat. Rev. Mol. Cell Biol 7, 813–819. [PubMed: 17006434]

Jaqaman K, Loerke D, Mettlen M, Kuwata H, Grinstein S, Schmid SL, and Danuser G (2008). Robust single-particle tracking in live-cell time-lapse sequences. Nat. Methods 5, 695–702. [PubMed: 18641657]

Jaqaman K, Kuwata H, Touret N, Collins R, Trimble WS, Danuser G, and Grinstein S (2011). Cytoskeletal control of CD36 diffusion promotes its receptor and signaling function. Cell 146, 593–606. [PubMed: 21854984]

Jaqaman K, Galbraith JA, Davidson MW, and Galbraith CG (2016). Changes in single-molecule integrin dynamics linked to local cellular behavior. Mol. Biol. Cell 27, 1561–1569. [PubMed: 27009207]

Jin ZG, Ueba H, Tanimoto T, Lungu AO, Frame MD, and Berk BC (2003). Ligand-independent activation of vascular endothelial growth factor receptor 2 by fluid shear stress regulates activation of endothelial nitric oxide synthase. Circ. Res 93, 354–363. [PubMed: 12893742]

Jonker R, and Volgenant A (1987). A Shortest Augmenting Path Algorithm for Dense and Sparse Linear Assignment Problems. Computing 38, 325–340.

Karaman S, Leppänen VM, and Alitalo K (2018). Vascular endothelial growth factor signaling in development and disease. Development 145, 8.

Kasai RS, Ito SV, Awane RM, Fujiwara TK, and Kusumi A (2018). The Class-A GPCR Dopamine D2 Receptor Forms Transient Dimers Stabilized by Agonists: Detection by Single-Molecule Tracking. Cell Biochem. Biophys 76, 29–37. [PubMed: 29116599]

King C, and Hristova K (2019). Direct measurements of VEGF-VEGFR2 binding affinities reveal the coupling between ligand binding and receptor dimerization. J. Biol. Chem 294, 9064–9075. [PubMed: 31023826]

Labrecque L, Royal I, Surprenant DS, Patterson C, Gingras D, and Béliveau R (2003). Regulation of vascular endothelial growth factor receptor-2 activity by caveolin-1 and plasma membrane cholesterol. Mol. Biol. Cell 14, 334–347. [PubMed: 12529448]

Lampugnani MG, Orsenigo F, Gagliani MC, Tacchetti C, and Dejana E (2006). Vascular endothelial cadherin controls VEGFR-2 internalization and signaling from intracellular compartments. J. Cell Biol 174, 593–604. [PubMed: 16893970]

Lecca P (2013). Stochastic chemical kinetics : A review of the modelling and simulation approaches. Biophys. Rev 5, 323–345. [PubMed: 28510113]

Lin C-C, Melo FA, Ghosh R, Suen KM, Stagg LJ, Kirkpatrick J, Arold ST, Ahmed Z, and Ladbury JE (2012). Inhibition of basal FGF receptor signaling by dimeric Grb2. Cell 149, 1514–1524. [PubMed: 22726438]

Linkert M, Rueden CT, Allan C, Burel JM, Moore W, Patterson A, Loranger B, Moore J, Neves C, Macdonald D, et al. (2010). Metadata matters: access to image data in the real world. J. Cell Biol 189, 777–782. [PubMed: 20513764]

Liu Z, Lavis LD, and Betzig E (2015). Imaging live-cell dynamics and structure at the single-molecule level. Mol. Cell 58, 644–659. [PubMed: 26000849]

Low-Nam ST, Lidke KA, Cutler PJ, Roovers RC, van Bergen en Hene-gouwen PM, Wilson BS, and Lidke DS (2011). ErbB1 dimerization is promoted by domain co-confinement and stabilized by ligand binding. Nat. Struct. Mol. Biol 18, 1244–1249. [PubMed: 22020299]

Manley PW, Furet P, Bold G, Brüggen J, Mestan J, Meyer T, Schnell CR, Wood J, Haberey M, Huth A, et al. (2002). Anthranilic acid amides: a novel class of antiangiogenic VEGF receptor kinase inhibitors. J. Med. Chem 45, 5687–5693. [PubMed: 12477352]

Mischel PS, Umbach JA, Eskandari S, Smith SG, Gundersen CB, and Zampighi GA (2002). Nerve growth factor signals via preexisting TrkA receptor oligomers. Biophys. J 83, 968–976. [PubMed: 12124278]

Mutch SA, Fujimoto BS, Kuyper CL, Kuo JS, Bajjalieh SM, and Chiu DT (2007). Deconvolving single-molecule intensity distributions for quantitative microscopy measurements. Biophys. J 92, 2926–2943. [PubMed: 17259276]

Olsson AK, Dimberg A, Kreuger J, and Claesson-Welsh L (2006). VEGF receptor signalling - in control of vascular function. Nat. Rev. Mol. Cell Biol 7, 359–371. [PubMed: 16633338]

Ruch C, Skiniotis G, Steinmetz MO, Walz T, and Ballmer-Hofer K (2007). Structure of a VEGF-VEGF receptor complex determined by electron microscopy. Nat. Struct. Mol. Biol 14, 249–250. [PubMed: 17293873]

Sarabipour S, Ballmer-Hofer K, and Hristova K (2016). VEGFR-2 conformational switch in response to ligand binding. eLife 5, e13876. [PubMed: 27052508]

Simons M, Gordon E, and Claesson-Welsh L (2016). Mechanisms and regulation of endothelial VEGF receptor signalling. Nat. Rev. Mol. Cell Biol 17, 611–625. [PubMed: 27461391]

Somanath PR, Malinin NL, and Byzova TV (2009). Cooperation between integrin alphavbeta3 and VEGFR2 in angiogenesis. Angiogenesis 12, 177–185. [PubMed: 19267251]

Sungkaworn T, Jobin ML, Burnecki K, Weron A, Lohse MJ, and Calebiro D (2017). Single-molecule imaging reveals receptor-G protein interactions at cell surface hot spots. Nature 550, 543–547. [PubMed: 29045395]

Terman BI, Dougher-Vermazen M, Carrion ME, Dimitrov D, Armellino DC, Gospodarowicz D, and Böhlen P (1992). Identification of the KDR tyrosine kinase as a receptor for vascular endothelial cell growth factor. Biochem. Biophys. Res. Commun 187, 1579–1586. [PubMed: 1417831]

Treanor B, Depoil D, Gonzalez-Granja A, Barral P, Weber M, Dushek O, Bruckbauer A, and Batista FD (2010). The membrane skeleton controls diffusion dynamics and signaling through the B cell receptor. Immunity 32, 187–199. [PubMed: 20171124]

Tzima E, Irani-Tehrani M, Kiosses WB, Dejana E, Schultz DA, Engel-hardt B, Cao G, DeLisser H, and Schwartz MA (2005). A mechanosensory complex that mediates the endothelial cell response to fluid shear stress. Nature 437, 426–431. [PubMed: 16163360]

Vega AR, Freeman SA, Grinstein S, and Jaqaman K (2018). Multistep Track Segmentation and Motion Classification for Transient Mobility Analysis. Biophys. J 114, 1018–1025. [PubMed: 29539390]

Xia T, Li N, and Fang X (2013). Single-molecule fluorescence imaging in living cells. Annu. Rev. Phys. Chem 64, 459–480. [PubMed: 23331306]

Zhou Y, Prakash P, Liang H, Cho KJ, Gorfe AA, and Hancock JF (2017). Lipid-Sorting Specificity Encoded in K-Ras Membrane Anchor Regulates Signal Output. Cell 168, 239–251.e16. [PubMed: 28041850]

Highlights

- VEGFR-2 exhibits motion and interaction heterogeneity on endothelial cell surface

- The steps of VEGFR-2 activation by VEGF depend on the basal state of VEGFR-2

- VEGF binds VEGFR-2 monomers and non-monomers on endothelial cell surface

- The effect of VEGF on VEGFR-2 dimerization varies by mobility of VEGFR-2 monomers
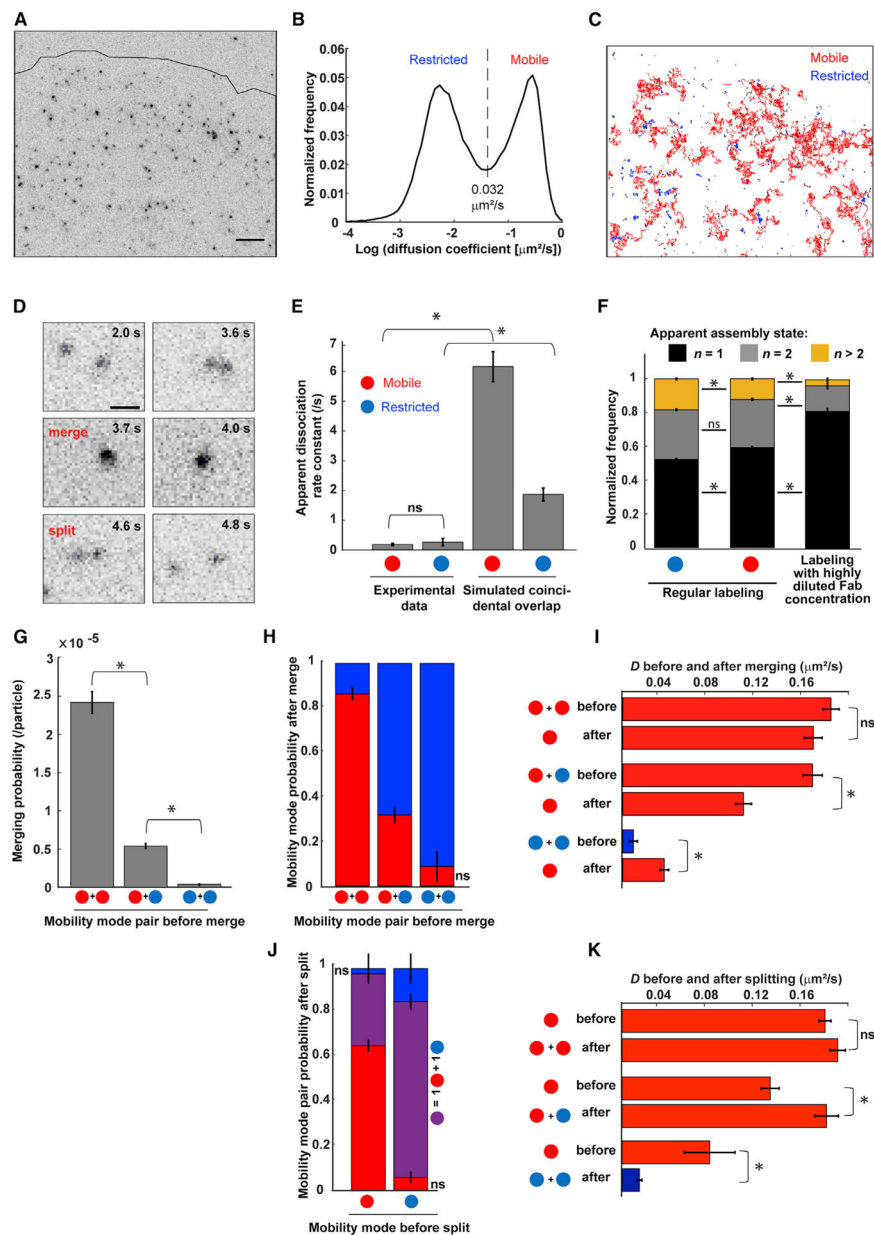
Figure 1. The Dynamic Organization of VEGFR-2 on the Surface of Unstimulated pHMVECs

(A) Representative single-molecule image of RRX-labeled endogenous VEGFR-2 on the surface of a pHMVEC, with cell outline delineation. Scale bar, 5 μm. The image is inverted for visual clarity.

(B) VEGFR-2 effective diffusion coefficient distribution. Vertical dashed line, threshold between the mobile and restricted modes.

(C) VEGFR-2 tracks over a 10-Hz/20-s SMI stream, colored based on mobility mode (red, mobile; blue, restricted; black, duration < 5 frames, hence too short to classify). Shown are the same cell and area as in (A).

(D) Series showing VEGFR-2 particle merging and splitting. Scale bar, 1 μm (all sub-panels). Images are inverted for visual clarity.

(E) Apparent dissociation rate constant for VEGFR-2 as observed experimentally ("experimental data") and from simulations of coincidental overlap within the resolution limit ("simulated coincidental overlap"; calculated by simulating non-interacting receptors that diffuse in 2D in a manner similar to VEGFR-2 and then obtaining the distribution of apparent fusion times caused by resolution limitations; Jaqaman et al., 2011). Red and blue circles represent mobile and restricted particles, respectively (also in F–K).

(F) Frequency of the apparent assembly state of detected VEGFR-2 particles in the two mobility modes and in samples with highly diluted labeling, with the latter reflecting the number of fluorophores per secondary Fab fragment.

(G) Probability of VEGFR-2 merging per combination of mobility modes.

(H) Probability of mobility mode for merged particle based on the particle mobility modes before merging. Red and blue bars indicate mobile and restricted modes, respectively (also in I–K).

(I) Comparison of D before and after merging events that produce a mobile particle. If the particles before merging are both mobile or both restricted, then the displayed D is the average of the two particles. If one particle is mobile and the other is restricted, then only the mobile particle D is shown.

(J) Probability of mobility modes for particles after splitting based on the mobility mode of the spitting particle. Purple bars indicate one mobile and one restricted particle.

(K) Comparison of D before and after splitting events that originate from a mobile particle. The analysis is equivalent to that shown in (I) but for splitting instead of merging.

Error bars in (E)–(K), standard deviation from 100 bootstrap samples. In (E)–(G), (I), and (K), *p < 0.005 when comparing between the indicated conditions (STAR Methods); ns, not significant (p > 0.05). In (H) and (J), ns (i.e., p > 0.05), the probability is not significantly different from 0. Probabilities without "ns" are significant. n: VEGFR-2, 140,445 tracks (53,417 with duration 5 frames) from 9 independent experiments with 7–9 cells each, yielding 1,328 merges and 1,515 splits; highly diluted sample, 8,751 tracks (2,200 with duration 5 frames) from 2 independent experiments with 10 cells each. See also Figure S1.
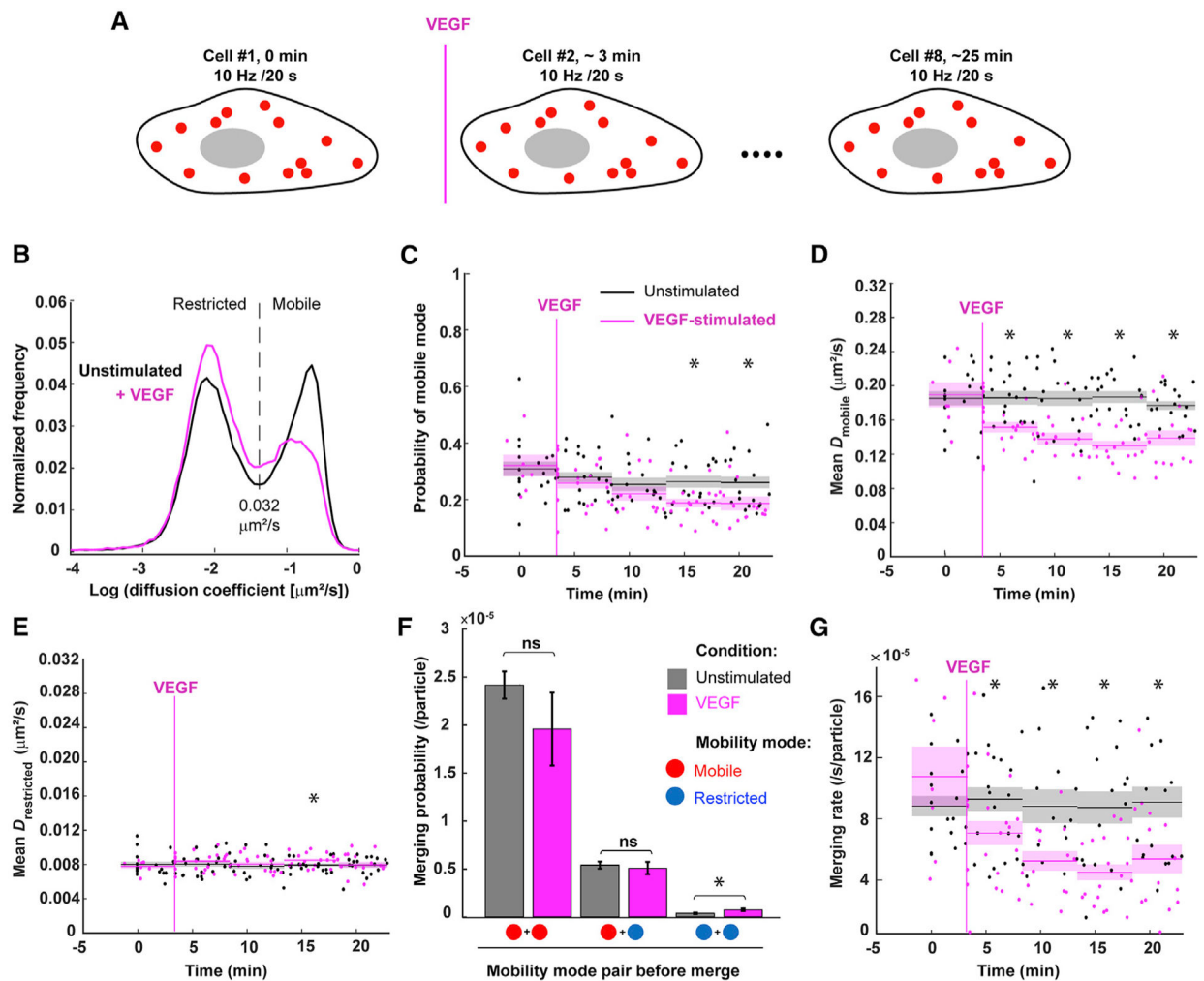
Figure 2. VEGF-Induced Changes in the Dynamic Organization of VEGFR-2 on the pHMVEC Surface

(A) Cartoon illustrating time course imaging.

(B) VEGFR-2 effective diffusion coefficient distribution on the surface of unstimulated (black) and 2 nM VEGF-stimulated (magenta) pHMVECs. Unstimulated distribution and vertical dashed line, repeat of Figure 1B.

(C–E) Time courses of the probability of VEGFR-2 molecules belonging to the mobile mode (C), mean D_{mobile} (D), and mean $D_{restricted}$ (E). Black and magenta, measurements from unstimulated and VEGF-stimulated time courses, respectively; vertical magenta line, mean time point of VEGF addition; dots, individual cell values; lines and surrounding shaded areas, the mean and standard error of the mean, respectively, from cells grouped into 5-min intervals as indicated. *p < 0.05 for comparing stimulated and unstimulated measurements per time interval using a t test. Time intervals without an asterisk, no significant difference (p > 0.05).

(F) Probability of VEGFR-2 merging per combination of mobility modes in cells stimulated (magenta) or not (gray) with 2 nM VEGF for 10–20 min. Error bars, standard deviations from 100 bootstrap samples. ns, p < 0.05; *p > 0.05 when comparing between the indicated conditions (STAR Methods).

(G) Time course of the rate of merging. All details as in (C)–(E).

n: unstimulated, same as in Figure 1; stimulated: 99,699 tracks (42,865 with duration 5 frames) from 8 independent experiments with 7–8 cells each, yielding 977 merges and 1,036 splits. See also Figure S2.
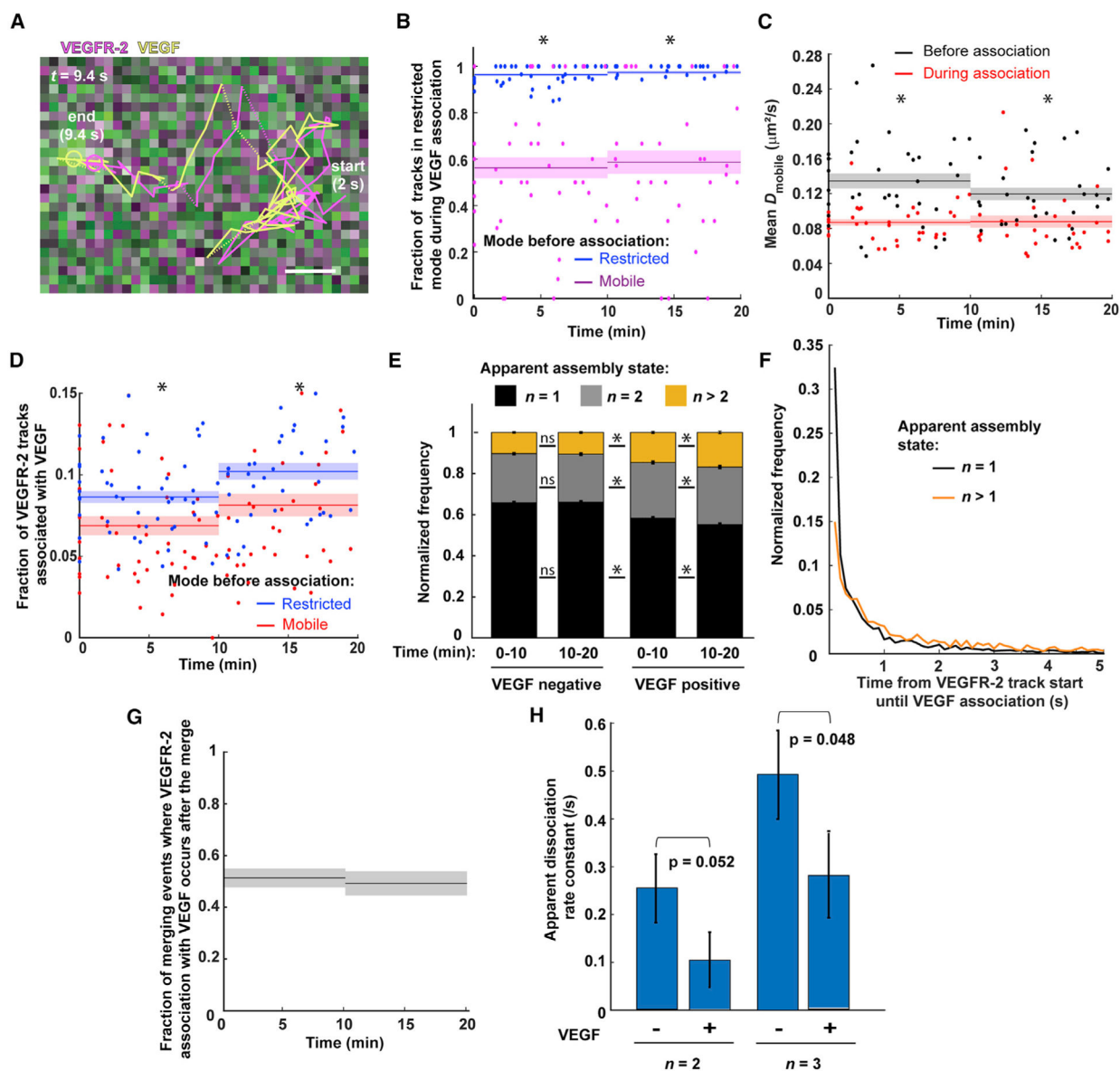
Figure 3. Dissection of the Relationship between Individual VEGFR-2 Molecules Associating with VEGF and Their Mobility and Interactions

(A) A track of RRX-labeled VEGFR-2 (magenta) and its associated Atto488-labeled VEGF (light green), overlaid on the merged image of the 561 (magenta) and 488 (green) channels in the last displayed frame (at 9.4 s). Scale bar, 500 nm. The VEGF track was constructed based on the association of VEGF with VEGFR-2, not by tracking VEGF particles directly.

(B) Time course of the fraction of VEGFR-2 tracks in restricted mode while associated with an Atto488-VEGF particle, per mobility mode before VEGF association. Dots, lines, and surrounding shaded areas are as in Figure 2C. *p < 0.01 for comparing the two measurements in each time interval using a t test.

(C) Time course of mean D_{mobile}, before and during VEGF association, for VEGFR-2 particles that are mobile before and during VEGF association. Details as in (B).

(D) Time course of the fraction of VEGFR-2 tracks associated with Atto488-VEGF per VEGFR-2 mobility mode before association. Details as in (B).

(E) Frequency of the apparent assembly state of detected VEGFR-2 particles associated (VEGF-positive) or not (VEGF-negative) with Atto488-VEGF, in the indicated time intervals. Error bars, standard deviations from 100 bootstrap samples. *p < 0.005; ns, p > 0.05 when comparing the corresponding frequencies between the indicated conditions (STAR Methods).

(F) Normalized frequency of wait times between the start of a VEGFR-2 track and its association with Atto488-VEGF for the subset of tracks that associate with VEGF after their first time point (23% of $n = 1$ tracks and 60% of $n > 1$ tracks).

(G) Time course of the fraction of merging events where VEGFR-2 association with Atto488-VEGF occurs after the merge. Lines and surrounding shaded areas, measured fraction and its standard deviation from 100 bootstrap samples.

(H) Apparent dissociation rate constant for VEGFR-2 associated (+) or not (−) with Atto488-VEGF, for $n = 2$ or $n = 3$ apparent assembly states. Error bars as in (E).

n: 189,097 tracks (81,188 with duration 5 frames) from 10 independent experiments with 6–8 cells each, yielding 1,655 merges and 1,737 splits. See also Figure S3.
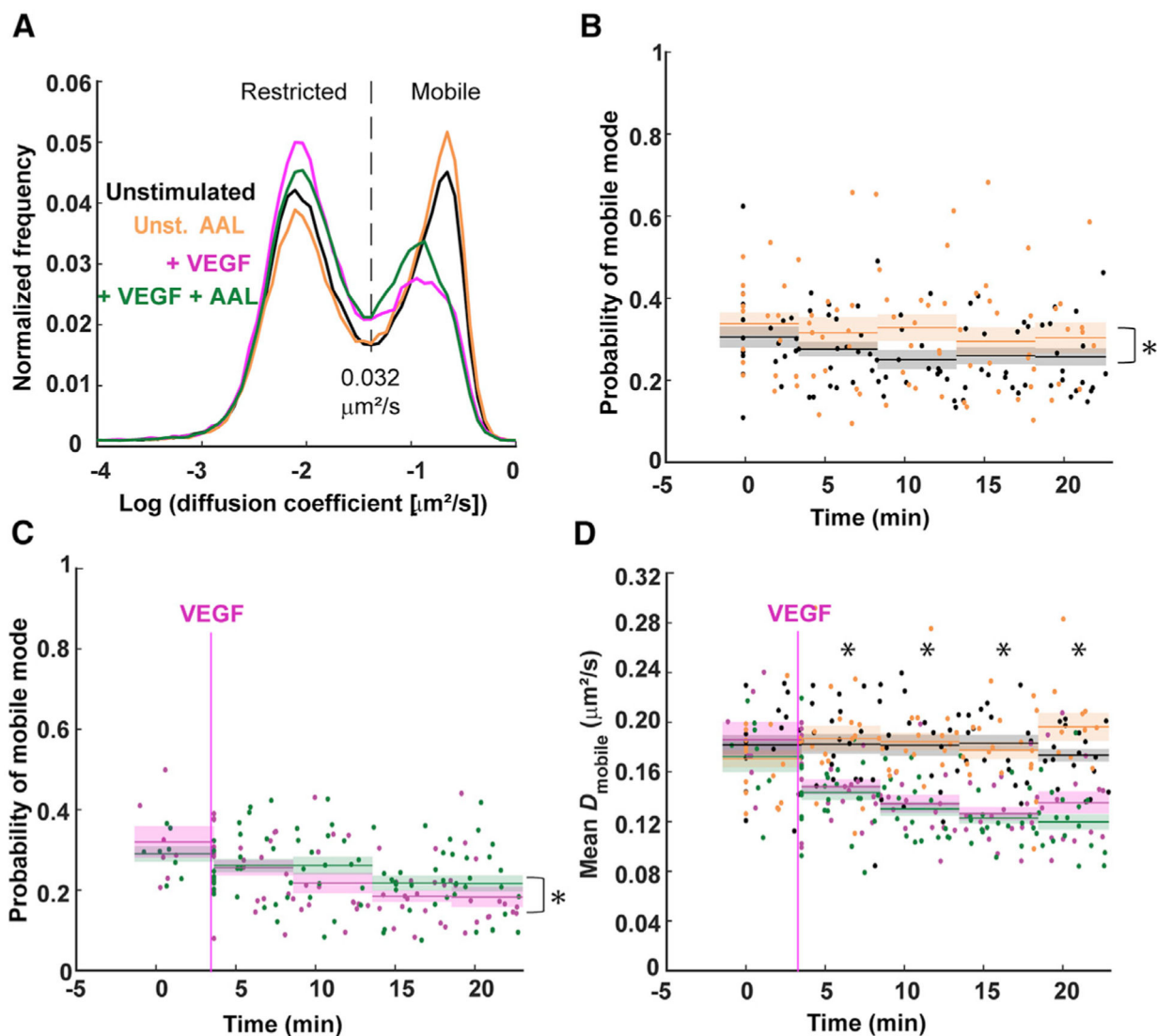
Figure 4. Effect of Phosphorylation Inhibition on the Dynamic Organization of VEGFR-2 on the pHMVEC Surface

(A) VEGFR-2 effective diffusion coefficient distribution on the surface of pHMVECs: unstimulated (black), stimulated with 2 nM VEGF (magenta), unstimulated in the presence of 30 nM AAL-993 (orange), and VEGF-stimulated in the presence of AAL-993 (green). Unstimulated and VEGF-stimulated (without AAL-993) distributions and vertical dashed line, repeat of Figure 2B.

(B–D) Time courses of the probability of VEGFR-2 molecules belonging to the mobile mode in unstimulated cells (B) and in VEGF-stimulated cells (C) in the absence or presence of AAL-993 and mean D_{mobile} for all conditions (D). Dots, lines, surrounding shaded areas, and vertical magenta line as in Figure 2C. In (B) and (C), *$p < 0.02$ for comparing the total time course between conditions using a paired t test (in C, the comparison is only for the time intervals after VEGF addition). In (D), *$p < 0.05$ for comparing the measurements with and without VEGF stimulation in the presence of AAL-993 per time interval using a t test.

n: unstimulated, same as in Figure 1; + VEGF, same as in Figure 2; unstimulated AAL, 133,815 tracks (48,851 with duration   5 frames) from 8 independent experiments with 7–9 cells each; AAL + VEGF: 134,371 tracks (54,198 with duration   5 frames) from 9 independent experiments with 7–8 cells each. See also Figure S3.

KEY RESOURCES TABLE

REAGENT or RESOURCE	SOURCE	IDENTIFIER
Antibodies		
Mouse monoclonal anti-VEGFR-2 (EIC)	Abcam	Cat# ab9530; RRID: AB_2234327
Goat anti-mouse Fab secondary fragment (Rhodamine-Red-X conjugated)	Jackson ImmunoResearch	Cat# 115–297-003 Lot# 142110; RRID: AB_2338784
Rabbit monoclonal anti-VEGFR-2 (55B11)	Cell Signaling Technology	Cat# 2479; RRID: AB_2212507
Rabbit monoclonal anti-phospho VEGFR-2 (Y1175)	Cell Signaling Technology	Cat# 2478; RRID: AB_331377
Mouse monoclonal anti-actin (AC40)	Millipore-Sigma	Cat# A4700; RRID: AB_476730
Rabbit polyclonal anti-GAPDH	Abcam	Cat# ab9485; RRID: AB_307275
Goat anti-Rabbit polyclonal antibody (HRP conjugated)	Thermo Scientific	Cat# G21234; RRID: AB_2536530
Chemicals, Peptides, and Recombinant Proteins		
VEGF-A$_{165}$ (VEGF)	GenScript	Cat# Z03073–50
AAL-993	Millipore-Sigma	Cat# 676504
Critical Commercial Assays		
Pierce Mouse IgG1 Fab and F(ab')2 Preparation Kit	Thermo Scientific	Cat# 44980
Atto Protein Labeling Kit	Millipore-Sigma	Cat# 38371
Experimental Models: Cell Lines		
Human Dermal Microvascular Endothelial Cells-Neonatal (HD-MVECn), passages 4 to 7	LifeLine Cell Technology	Cat# FC-0042
Software and Algorithms		
MATLAB	The MathWorks	https://www.mathworks.com/
Bio-formats	Linkert et al., 2010	https://www.openmicroscopy.org/bio-formats/
u-track	Jaqaman et al., 2008	https://github.com/DanuserLab/u-track
diffModesF2F	Jaqaman et al., 2016	https://github.com/kjaqaman/diffModesF2F
FISIK	de Oliveira and Jaqaman 2019	https://github.com/kjaqaman/FISIK
timeCourseAnalysisPlus	This work	https://github.com/kjaqaman/timeCourseAnalysisPlus
Includes:		
Basic time course analysis		
Merging/splitting/motion analysis		
Primary-secondary channel analysis		